

Finite Element Modeling of the Electrical Impedance Tomography Technique Driven by Machine Learning

Mohamed Elkhodbia^a, Imad Barsoum^{a,b,c,*}, Feras Korkees^d, Shrinivas Bojanampati^a

^a*Department of Mechanical Engineering, Khalifa University of Science and Technology, Abu Dhabi, 127788, UAE*

^b*Department of Engineering Mechanics, Royal Institute of Technology – KTH, Teknikringen 8, Stockholm, 100 44, Sweden*

^c*Advanced Digital and Additive Manufacturing Research Centre, Khalifa University of Science and Technology, Abu Dhabi, 127788, UAE*

^d*Materials Research Centre, Swansea University, Swansea, SA2 8PP, UK*

Abstract

To create a human-like skin for a robotic application, current touch sensor technologies have a few drawbacks. Electrical Impedance Tomography (EIT) is a candidate for this application due to its applicability over complex geometries; nevertheless, it has accuracy concerns. This study employs artificial neural networks (ANNs) to investigate the accuracy and capability of EIT-based touch sensors. A finite element (FE) model is utilized to solve the forward EIT problem while simultaneously determining the system's comprehensive mechanical response. The FE model is comprised of a polyurethane (PU) foam domain, a conductive spray layer and a set of sixteen electrodes. To replicate the process of touching the sensor body, a punch of varying diameters and touch forces is utilized. The mechanical response of the sensor body is modeled using the hyperfoam material model calibrated through experimental uniaxial and shear test data, while the electric conductivity of the sprayed skin surface is obtained experimentally as function of applied strain. The viscoelastic behavior of the PU foam material is also obtained experimentally. These experimental data were implemented in the FE model through user subroutines to model the mechanical and electrical properties of the sensor in the EIT forward problem. The traditional EIT inverse prob-

*Corresponding author

Email address: `imad.barsoum@ku.ac.ae` (Imad Barsoum)

lem image reconstruction was replaced utilizing ANNs as an alternative to extract mechanics based parameters. The ANNs were created to predict the spatial coordinates of the touch point, and they were proven to be extremely accurate. Using the EIT voltage readings as input, the ANNs were utilized to forecast the system’s mechanical behavior such as contact pressure, contact area, indentation depth, and touching force.

Keywords: Electrical impedance tomography, Machine learning, Electrical conductivity, Finite element analysis, Tactile sensor

1. Introduction

1.1. Background

Adding a sense of touch to robots has been one of the most sought-after additions in the robotics industry, and tactile sensors provide the means to implement such feature. Tactile sensors are sensors that can detect touch and contact, estimate grip forces, detect motion, and perceive both dynamic and static forces. Several tactile sensor technologies, including magnetic, piezoelectric, capacitive, and optical sensors, have been implemented in the robotics industry. When applied to robotic skins, however, these tactile sensing technologies have two significant limitations. First, their high cost for relatively large robots, which is a result of both the number of sensors required to create a sensory map across the robot’s surface and the number of batteries required to power a large sensor area. The second limitation of tactile sensors is their inability to be applied to complex geometries, such as joints, due to their stiffness and wiring requirements [1].

Electrical impedance tomography (EIT) is a cost-effective imaging technology that overcomes certain limitations in sensor design by deducing applied stimuli based on boundary data to estimate the internal conductivity map of a sensor domain [1]. While both EIT and electrical resistance tomography (ERT) capture conductivity distributions, EIT additionally measures permittivity profiles using alternating current. Despite their differences, past research [2, 3] often refers to ERT as EIT, a practice this paper will follow when discussing the exclusive retrieval of conductivity distribution. In general, EIT systems involve a conductive domain with boundary electrodes subjected to varying current injection patterns. As depicted in Figure 1, each pattern injects current through one electrode while another serves as the sink. The domain exhibits distinct voltage values as the current flows,

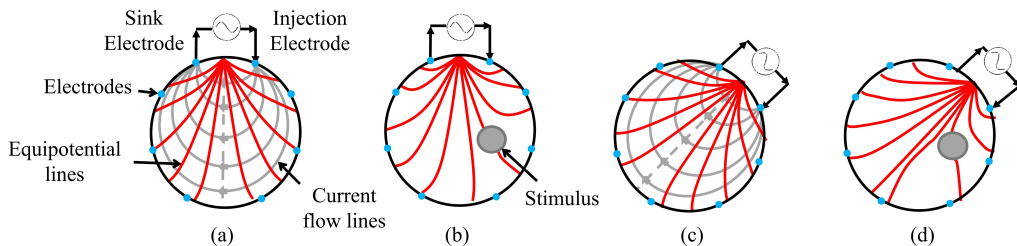


Fig. 1: (a) The equipotential lines for a domain without any change in the internal conductivity map for the first current injection pattern, (b) an object with different conductivity value in contact with the domain and its affect on the internal conductivity distribution, (c) and (d) show the same phenomenon for a different current injection pattern.

with boundary electrodes monitoring these potentials. Upon interaction with a stimulus, changes in the domain’s internal conductivity map cause current flow redirection and potential variation at the boundary electrodes. An EIT solver can then ascertain the internal conductivity distribution using these boundary measurements.

The EIT problem encompasses two parts, the forward problem and the inverse problem. Solving the forward problem means computing the potential distributions across the entire domain. Due to the problem’s complexity and complex boundary conditions, the complete electrode model (CEM), a solution requires the use of numerical method such as the finite element method (FEM) [1, 4, 5, 6]. The inverse problem, however, involves reconstructing the internal conductivity distribution from boundary measurements - a task complicated by its nonlinearity and sensitivity to small changes in measurements [1]. Conventional approaches to navigate these intricacies typically incorporate either static [7] or dynamic [8] imaging techniques (c.f. Holder [8]).

1.2. EIT Sensing and Machine Learning

While EIT provides valuable information about internal conductivity, its direct applicability may be less straightforward in fields such as robotics, where mechanical factors such as pressure, contact area, force distribution, or stretch often play a more crucial role. As a result, recent years have witnessed a surge of interest in the application of EIT for predicting mechanical behaviors. For instance, it has been applied to infer strain states in nanocomposites by tracking conductivity changes [9], and to model displacement fields

as well as derive stress-strain relationships using conductivity data [10]. Furthermore, it has been effectively utilized for monitoring moisture flow and identifying damages in concrete structures [11, 12].”

Utilizing EIT image reconstruction for such applications, however, is not without its challenges. The main obstacle is solving an inverse problem which is highly sensitive to noise and changes in boundary potential readings, leading to potential errors and lower reconstruction quality. Furthermore, establishing a constitutive relationship between changes in conductivity and mechanical response introduces an added layer of complexity to the process. The initial approach to address these problems began with a gradient-based optimization technique developed by Tallman and Wang [9, 10]. The objective was to reduce the difference between observed and computed conductivity distributions. However, this method proved insufficient in certain scenarios. The Genetic Algorithm (GA), a meta-heuristic global search algorithm, was introduced to address these complexities [2]. While the GA effectively estimates the mechanical response, it also results in discrepancies due to predicted displacement variations. Amongst various meta-heuristic algorithms such as Simulated Annealing (SA) and Particle Swarm Optimization (PSO), GA was identified as the most effective [13]. Current research advancements have been inclining towards integrating machine learning with EIT to optimize various aspects of the methodology. For instance, Neural networks (NNs) have been employed to reconstruct damage patterns in concrete [14]. Deep machine learning techniques have been utilized for real-time touch sensing [15], reconstructing simulated CT scans of lungs [16], and improving electrode placement for better measurements [17]. There are also instances of research that deviate from the traditional EIT inverse solution, preferring direct machine learning methodologies instead. These approaches aim to leverage the power of artificial neural networks (ANNs) and deep learning techniques to directly address the challenges of EIT. For instance, researchers have successfully employed a single perception ANNs to directly predict the location and magnitude of damage in EIT applications [18]. Deep neural networks (DNNs) have been utilized for image reconstruction in EIT, enabling accurate reconstructions of simulated CT scans and challenging shape reconstructions using specific geometric data [19, 20]. Deep learning frameworks have shown promise in directly predicting strain and stress distributions [21]. These approaches have demonstrated the potential of both simple ANNs and complex DNNs, in addressing the complexities of EIT and enabling mechanics reconstructions from conductivity maps.

In this study, we present a computational framework for robotic skin sensors based on EIT. Our machine learning approach focuses on predicting specific tactile parameters, including touch location, contact pressure, area, indentation depth, and force, instead of full-domain reconstruction. We generate the training data for these predictions through a rigorous process of mechanical-electrical FEA applied to a very large number of randomized scenarios.

2. Material Selection and Conductivity Modeling for EIT Sensors

2.1. EIT Material Considerations

In the larger scope of EIT, structures used are generally classified into two categories. The first comprises of inherently self-sensing materials, including structures like CNT-coated fabric-reinforced polymers [3] and carbon nanofiber/epoxy matrices [22]. The second category embraces structures that, while not inherently self-sensing, leverage multifunctional materials like skins, layers, or films as their sensing medium [23, 24, 12, 25, 26].

Moreover, an important aspect of enhancing the accuracy of EIT sensors is the choice of materials with good stretchability, conductivity, low cost and weight [1]. Human skin, with its intricate functions such as sensitivity to touch, pressure, and temperature, serves as an inspirational model for material selection. The skin’s viscoelastic properties protect the human body from injuries while allowing us to perceive our surrounding environment, making it a remarkable natural sensor. This serves as the motivation for our work with EIT sensors, which can be implemented in areas such as robotics, where the need to shield sensitive components during the process of sensing external conditions is crucial. Polyurethane (PU), a material frequently used to emulate the mechanical behavior of human skin, is particularly noteworthy [27, 28]. The properties of PU can be fine-tuned depending on the application by varying foam ratios and additives. PU foam, a subtype of polyurethanes known for its low Poisson’s ratio and hyperelastic behavior, has been successfully utilized in EIT tactile distribution sensors [29], thus validating its suitability as an EIT-compatible material.

2.2. Piezoresistive Models

Incorporating the effect of changes in the electrical conductivity of the sensor material due to deformation in the EIT forward problem could improve the reconstruction quality [1]. To predict conductivity changes under

various strains, a range of strain-to-conductivity models are employed depending on the context and material in question. Most models are based on percolation theory, which may predict the link between composite conductivity and conductive filler content by assuming that conductive particles form a conductive three-dimensional network [30]. The increase in resistance under tensile strain is associated with the three-dimensional conductive network being repeatedly broken and reformed, undergoing contact loss between conductive particles, and approaching the percolation threshold [31, 30]. For the case of self-sensing materials such as nanocomposites, a variety of models have been adopted. At the microscale, equivalent resistor network models are often employed [32, 33]. These models depict nanofillers as discretized resistor elements, providing micro-level insights into the piezoresistive behavior of the material. On the other hand, computational micromechanics models [34, 35] operate within a FEA framework, simulating the intricate interaction between nanofillers and the matrix material. This approach is particularly adept at incorporating various mechanical effects. For a broader perspective, analytical models [36, 37] are also employed. These models operate across multiple scales, linking conductivity to parameters such as strain and manufacturing data, offering a computationally efficient method for comprehensive analyses. Another way for modelling piezoresistivity at a macroscale is to use a phenomenological gray box approach to explain the relation between the resistance and strain. This type of modelling is usually used when the scope is to find a bulk response of sensors [38, 39]. An example of such a model is the continuum piezoresistivity model used by Kim et al. [40], which models the evolution of resistivity of the MWCNT/TPU composite in a continuum sense, with resistivity parameters depending on deformation and assuming isotropic resistivity tensor.

In view of the aforementioned studies, our primary sensor material is chosen to be PU foam. In order for the sensor to meet the conductivity requirements it is coated with a conductive spray layer. This approach is aligned with the category of EIT sensors made of non-inherently conductive materials. Given our aim of incorporating the conductivity changes due to the macroscopic mechanical deformation, we adopt a macro-scale continuum piezoresistivity model, as a simplified approach choice mindful of the uncertainty around applying self-sensing models to our sensor.

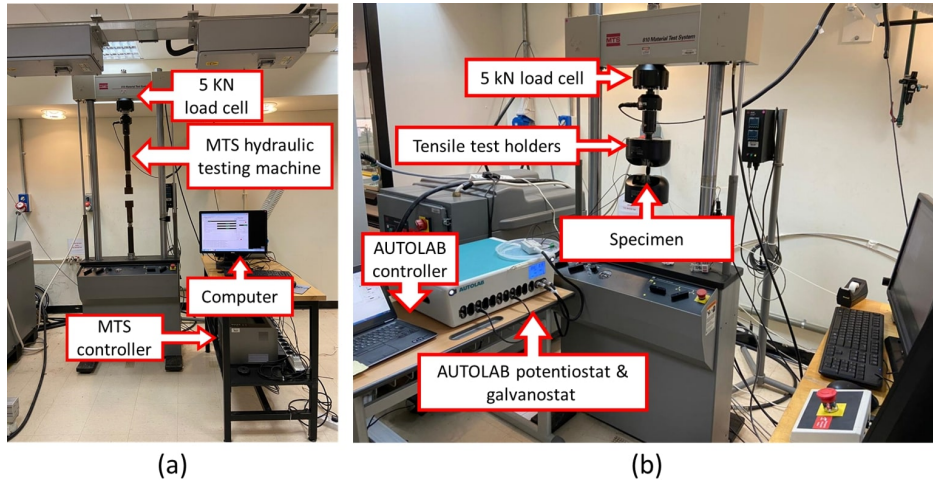


Fig. 2: (a) Experimental setup used for quasi-static uniaxial compression and compression relaxation tests, and (b) experimental setup used for capturing electrical conductivity change under deformation.

3. Experimental Methodology and Results

Given the choice of the sensor’s material and the computational nature of this study, both the behaviour of PU foam and the effect of stretch on electrical conductivity are required to be quantified. As a result, a variety of experiments are conducted to characterize the PU foam’s behavior and the sensor structure’s electro-mechanical behavior.

3.1. Mechanical Testing of PU Foam

In order to characterize the PU foam mechanical behavior, uniaxial compression tests, simple shear tests and compression relaxation tests were conducted. The experimental setup used for the compression and the compression relaxation tests are shown in fig. 2 (a).

PU foam provided by EUROPUR was utilized and tested in quasi-static uniaxial compression, shear and compression relaxation tests to characterize the mechanical behavior of the foam. All tests were conducted following the standards ISO 1827 [41], ISO 3384-1 [42] and ISO 3386-1 [43]. Quasi-static compression uniaxial test was carried out on round foam samples with dimensions of $50 \text{ mm} \pm 1 \text{ mm}$ diameter and a thickness of $20 \text{ mm} \pm 1 \text{ mm}$, as shown in fig. 3 (a). Then, the test pieces were compressed using a 5 kN load cell attached to an MTS hydraulic testing machine with a displacement

rate of 5 mm/min. Foam samples with the same size as the quasi-static compressive uniaxial test were tested for stress relaxation. The samples were deformed to 0.8 strain in 1 second, after which the deformation was kept fixed and the sample is let to relax for 180 seconds while the relaxation force is monitored, as shown in fig 5 (a). Notably, the strain measure used in this study is the nominal strain which is a common strain measurement used for calibrating various hyperelastic constitutive models for foam materials [44, 45, 46].

A simple quasi-static shear lap sample was developed following ISO 1827 [41], as shown in fig. 4 (a), to test the PU foam at a displacement rate of 5 mm/min with a sample size of 25 mm in length, 20 mm in width and 10 mm in thickness. An average shear stress is obtained as the ratio between the load cell force value and the total net-section shear area (4 faces each measuring 25 mm x 20 mm making a total area of 2000 mm²) and shear strain is obtained as the ratio between the displacement measurements and sample thickness.

Experimental stress-strain test results for the PU foam are displayed as solid markers in fig. 3 (b) and fig. 4 (b) for the quasi-static compression and shear test, respectively. Similarly, the normalized relaxation experimental results, e.g. normalized stress vs. time, are depicted in fig. 5 (b) with solid markers. These experimental results will be used to calibrate the hyperfoam model and the viscoelastic stress relaxation model in order to describe the constitute behavior of the PU foam such that its mechanical response is accurately predicted when subjected to loading through a stimulus. The calibration of the constitutive model is outlined in the next section.

3.2. Electric Conductivity Measurements

The experimental setup for measuring the effect of mechanical strain on electrical conductivity in the current study, as shown in fig. 2 (b), is similar to the one outlined by Kost et al. [47, 48, 49]. The MTS hydraulic testing machine is used for achieving the stretch in the sample and a potentiostat from AUTOLAB is used to capture the electric resistivity during stretching. PU foam samples, shown in fig. 6 (a) with dimensions 75 × 25 × 10 mm, were cut and their outer surfaces were sprayed with graphite conductive coating spray (e.g. Kontakt Chemie Graphit 33). Four pieces of plexiglass were cut and glued to the ends of the samples as insulation during electric resistivity measurements under tensile stretch. Using the two-point measurement method, two copper strips were attached to each end of the samples to

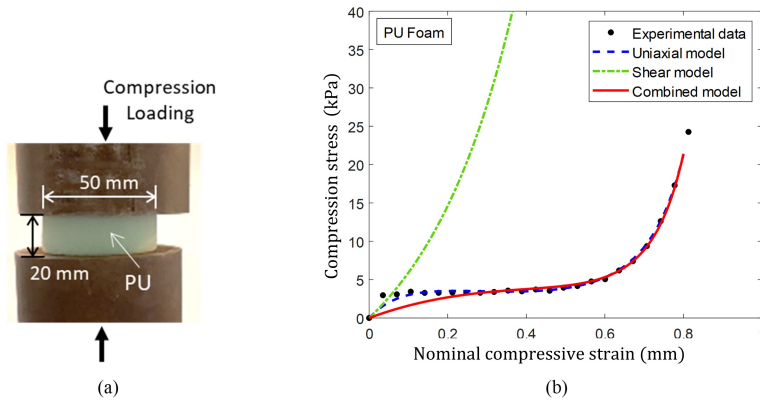


Fig. 3: Experimental results of the quasi-static compressive uniaxial test compared against uniaxial based, shear based and combined tests based hyperfoam models.

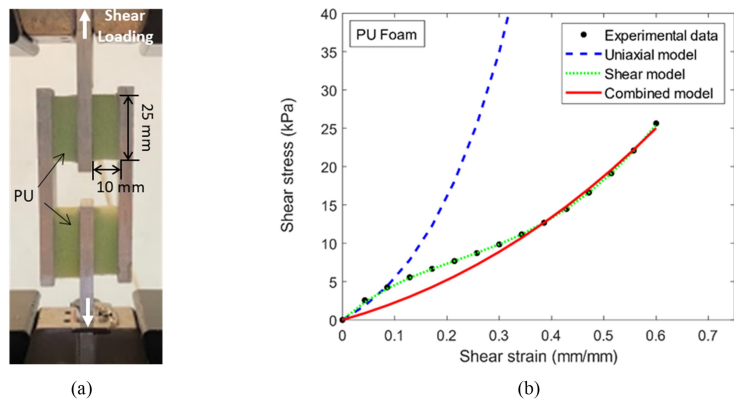


Fig. 4: Experimental results of the simple shear test compared against uniaxial based, shear based, and combined tests based hyperfoam models.

measure the electric resistivity.

The samples were tested in two stages. In the first stage, the samples were cyclically deformed with a displacement rate of 5 mm/min to a maximum stretch displacement of 4 mm and simultaneously subjected to a constant voltage of 0.5 V, while measuring the current. The resistance is determined using Ohm's law and the results are shown in fig. 6 (b) pertaining to the

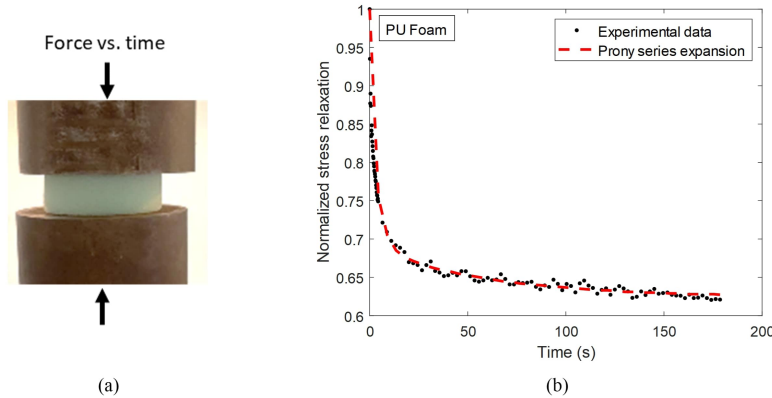


Fig. 5: Experimental results of the compressive stress relaxation test compared against a third order Prony series fit.

applied cyclic strain and measured resistance over time. As expected, the resistance decreases with each stretch cycle, and eventually reaches a steady value, which is consistent with the observation reported by Sevkati et al. [50]. In the second stage of the testing, and after the sample has been cycled reaching a steady value of resistance, the sample is stretched until failure, while simultaneously measuring the resistance with respect to stretch. The electric conductivity is calculated as $c = \frac{L}{RA}$, where R is the measured resistivity, L is the conductive sample length and A is the conductive sample cross sectional area. Notably, the value of A considered in the calculation of conductivity refers to the annular rectangular cross-sectional area formed by the conductive coating on the specimen, as depicted in fig. 6 (a). Moreover, fig. 6 (c) reveals that the conductivity decreases with increase in tensile stretch (e.g. positive strain), which is attributed to the continual breaking of the conductive network of the sprayed foam surface and is consistent with findings in literature [31, 30]. In contrast, it is reasonable to assume here that conductivity increases with increase in compressive strain due to the increase in contact interaction between the foam's conductive particles.

Due to limitations in the test setup used, obtaining the conductivity behavior under compression loading is not possible. Thus, the conductivity is extrapolated via a curve-fitting procedure for compression loading. A third order polynomial was used for the curve-fitting procedure to account for the nonlinearity in the experimental tensile-data and to show that compression

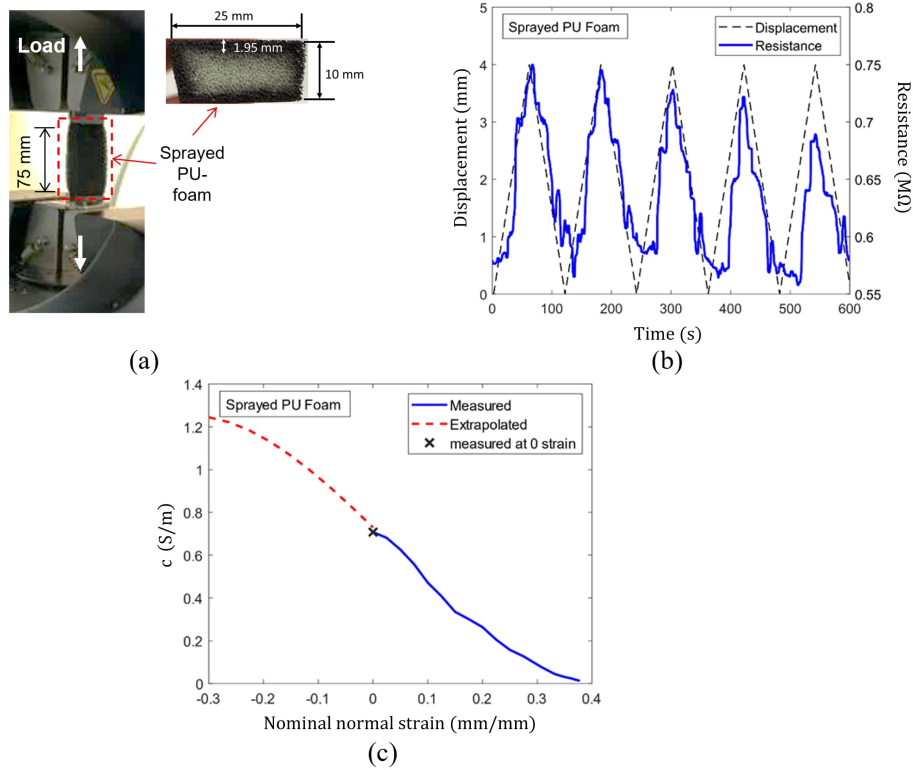


Fig. 6: (a) PU foam sample with conductive spray, (b) change in the resistance under 4 mm cyclic stretch along with a plot of the cyclic displacement applied to the sample, and (c) change in conductivity with respect to strain.

leads to higher conductivity conveniently. The relation between conductivity and strain, as indicated fig. 6 (c), is accounted for in the numerical solution to the EIT forward problem. Notably, the compressive strain values applied in this study are quite low, so, it is believed that curve-fitting extrapolation procedure is permissible.

4. Modeling EIT Forward Problem

The finite element method is well suited for solving the EIT forward problem and there are several toolboxes that can be utilized for this purpose. EIDORS [51] is a Matlab toolbox that can solve both the forward and inverse problems, while it is mostly utilized for the solution to the EIT inverse problem. Fouchard et. al. [4] utilized Comsol to solve the forward

problem, while other researchers [18, 52] employed the general purpose finite element package Abaqus [53] to solve the EIT forward problem. In the current study the heat transfer capability established in Abaqus is utilized, and the thermal-electrical conduction analogy is adopted to solve the EIT forward problem. The equivalency between the steady-state heat and the electric conduction governing equations is realized by

$$c \nabla^2 V = 0 \quad \rightarrow \quad k \nabla^2 T = 0 \quad (1)$$

where voltage V is the equivalency to temperature T , electric conductivity c is equivalent to thermal conductivity k , and ∇ is the gradient operator. Electric current sources and sinks are equivalent to heat sources and sinks, and the voltage ground electrode is equivalent to zero-temperature thermal boundary condition. This will enable the modeling of the coupled electro-mechanical EIT forward problem, e.g. through the thermo-mechanical equivalency, allowing to account for both the change in electrical conductivity and mechanical deformation of the EIT sensor, simultaneously, when a stimulus is applied. In addition, the CEM is a crucial component of the electrical component in the simulated mechanical-electrical EIT framework. This model takes into account the complexities of electrode behavior in the system. The model accommodates for a finite number of electrodes of specific size, considers the effect of conductive electrode shunting effect, and factors in the potential drop caused by the electrode's contact impedance. For more information on the mathematical formulation of the CEM, readers are referred to [1, 8].

4.1. Hyperelastic Constitutive Behavior

The core material of the EIT sensor considered in this study is a PU foam, and its constitutive material behavior is usually modelled with a hyperelastic material models, which are commonly used for accurately characterizing deformation of polymeric materials [54]. Various hyperelastic material models can be adapted such as the Ogden model [55], the Yeoh [56] and Neo-Hookean [57]. However, PU foam has a rather low Poisson's ratio [29] and is a rather compressible polymer [54], for which the most suitable hyperelastic model is the so called hyperfoam model [44, 46]. Here a third order hyperfoam material model is considered to model the combined compressive and shear mechanical response of the PU foam. The nominal compression stress (σ) of the specimen under uniaxial compression loading is calculated using the

hyperfoam constitutive model [44], and is given by

$$\sigma = \frac{2}{\lambda_1} \sum_{i=1}^N \frac{\mu_i}{\alpha_i} (\lambda_1^{\alpha_i} - J^{-\alpha_i \beta_i}) \quad (2)$$

where N is the order of fitting (e.g. $N = 3$), μ_i , α_i and β_i are material parameter obtained through curve-fitting, λ_1 , corresponds to the stretch ratio in the direction of axial compression load given by $\lambda_1 = 1 + \varepsilon_1$ (ε_1 is nominal strain), and $J = \lambda_1 \lambda_2 \lambda_3$ is the volume ratio given by the product of the principal stretch ratios. Due to the cylindrical shape of the PU foam specimen, as displayed in fig. 3 (a), it is here assume that the transverse stretch ratios are equal and rather negligible during the axial compression test, e.g. $\lambda_2 = \lambda_3 = 1$, suggesting that the Poisson's ratio $\nu = 0$. Hence, the material parameter β_i can be obtained through $\beta_i = \nu_i / (1 - 2\nu_i)$, and since $\nu_i = 0$ we obtain that $\beta_i = 0$. Similarly, the shear stress (τ) in the simple shear stress test, depicted in fig. 4 (a), is calculated using the hyperfoam constitutive model and is given by

$$\tau = \sum_{j=1}^2 \left[\frac{2\gamma}{2(\lambda_j^2 - 1) - \gamma^2} \sum_{i=1}^N \frac{\mu_i}{\alpha_i} (\lambda_j^{\alpha_i} - 1) \right] \quad (3)$$

where γ is the nominal shear strain, λ_1 and λ_2 are the two principal stretches in the plane of shearing and related to the shear strain by

$$\lambda_{1,2} = \left(1 + \frac{\gamma^2}{2} \pm \gamma \left(1 + \frac{\gamma^2}{4} \right)^{1/2} \right)^{1/2} \quad (4)$$

The material parameters μ_i and α_i are determined through a least squares optimization process using experimental data and eqns. (2)-(4) for the compressive uniaxial test alone, the shear test data alone and for both datasets concurrently. Fig. 3 (b) shows the compressive stress data and the corresponding models. The model based on shear experimental data is unstable, whereas the model based on uniaxial data offers the best fit. Similarly, fig. 4 (b) depicts the simple shear experimental data along with the corresponding material models. The results for the combined model in fig. 3 (b) and fig. 4 (b), where the hyperfoam model parameters in eqns. 2)-(4 are obtained by a simultaneous least-square fit to both the uniaxial compression and shear

Table 1: Hyperfoam and Prony series material model parameters ($N = 3$) for the PU foam.

i	μ_i [kPa]	α_i	β_i	τ_i^G	\bar{g}_i^p
1	14.42	0.288	0	0.2936	0.1505
2	16.78	4.249	0	5.8500	0.1696
3	-21.67	0.741	0	81.672	0.0604

dataset, capture the overall behavior of the PU foam rather accurately. The hyperfoam material model parameters (e.g. μ_i , α_i and $\beta_i = 0$) for the combined model are provided in table 1.

4.2. Viscoelastic Constitutive Behavior

As can be noted from experimental stress relaxation data in fig. 5 (b), depicting the normalized compressive stress over time, the relaxation behavior of the PU foam material is pronounced and it is necessary to account for this phenomenon when modeling the EIT sensor. In conjunction with the hyperfoam model, the stress relaxation behavior is modelled through a Prony series expansion of a third order ($N = 3$) given by

$$G(\tau) = G_o \left[1 - \sum_{i=1}^N \bar{g}_i^p (1 - e^{-\frac{\tau}{\tau_i^G}}) \right] \quad (5)$$

where G is the shear relaxation modulus, G_o is the initial shear modulus, τ is time, τ_i^G and \bar{g}_i^p are material constants [54, 58] obtained through a least square fitting procedure to the experimental relaxation data. fig. 5 (b) shows the experimental normalized stress relaxation data and the relaxation behavior as predicted with the calibrated Prony series model indicating a rather good agreement. The corresponding calibrated Prony series material parameters (e.g. τ_i^G and \bar{g}_i^p) for the PU foam are given in table 1. Thus, the constitutive behavior of the PU foam in the EIT sensor is modeled through the calibrated hyperfoam material model, allowing for stress relaxation through the Prony series as given in table 1.

4.3. Continuum Piezoresistive Model

The conductivity in the EIT model is assumed to vary with strain and given by the conductivity tensor \mathbf{c} , which is assumed to be isotropic and

given a Cartesian coordinate system by

$$\mathbf{c} = c \begin{bmatrix} 1 & 0 & 0 \\ 0 & 1 & 0 \\ 0 & 0 & 1 \end{bmatrix} \quad (6)$$

where c denote the electrical conductivity that depend on strain. The conductivity c is set as a function of the normal stretch ratio and fitted to the experimental conductivity-strain curve depicted in fig. 6 (c). This simplified strain-conductivity model was adopted due to the complexity of obtaining multiaxial experimental conductivity data.

4.4. Finite Element Model

The three dimensional finite element model developed to model the EIT forward problem is shown in fig. 7 (a), which resembles a typical EIT configuration [1]. The EIT skin sensor model is made of a $2r = 200$ mm diameter and 10 mm thickness PU foam, with a total of sixteen electrodes to enable injection of current and measurement of voltage as indicated in fig. 7 (a). The constitutive behavior of the EIT sensor is modelled as hyperelastic material with viscoelastic relaxation behavior as per the calibrated hyperfoam and Prony series model (e.g. table 1). The top surface of the PU foam is modelled as a conductive layer, assigned a strain-dependent electric conductivity given by the measurements in fig. 6 (c), while the remaining volume of the PU foam is considered electrically non-conductive. The assignment of the strain-dependent electric conductivity is accomplished through Abaqus user-defined Fortran subroutine USDFLD, which enables the user to specify a field variable at a material point as a function of time and the finite element solution. This subroutine was used to adjust the conductivity of the top surface of the EIT skin in response to the strain in the skin (c.f. fig. 6).

Fig. 6 shows the EIT sensor model with all the sixteen electrodes, cylindrical steel stimulus, and two different cases with random positions (x_0, y_0) and diameters d of the cylindrical steel punch. A cylindrical steel punch with various diameter sizes (e.g. $10 \leq d \leq 18$ mm) is adapted as the stimulus in the simulations, as shown in fig. 6 (a), which is modeled as an elastic material with a Young's modulus 210 GPa, Poisson's ratio 0.3 and constant conductivity 10×10^6 S/m, while the copper electrodes have a Young's modulus 110 GPa and constant conductivity 58×10^6 S/m. The cylindrical steel punch is randomly placed on the EIT sensor top surface at each simulation,

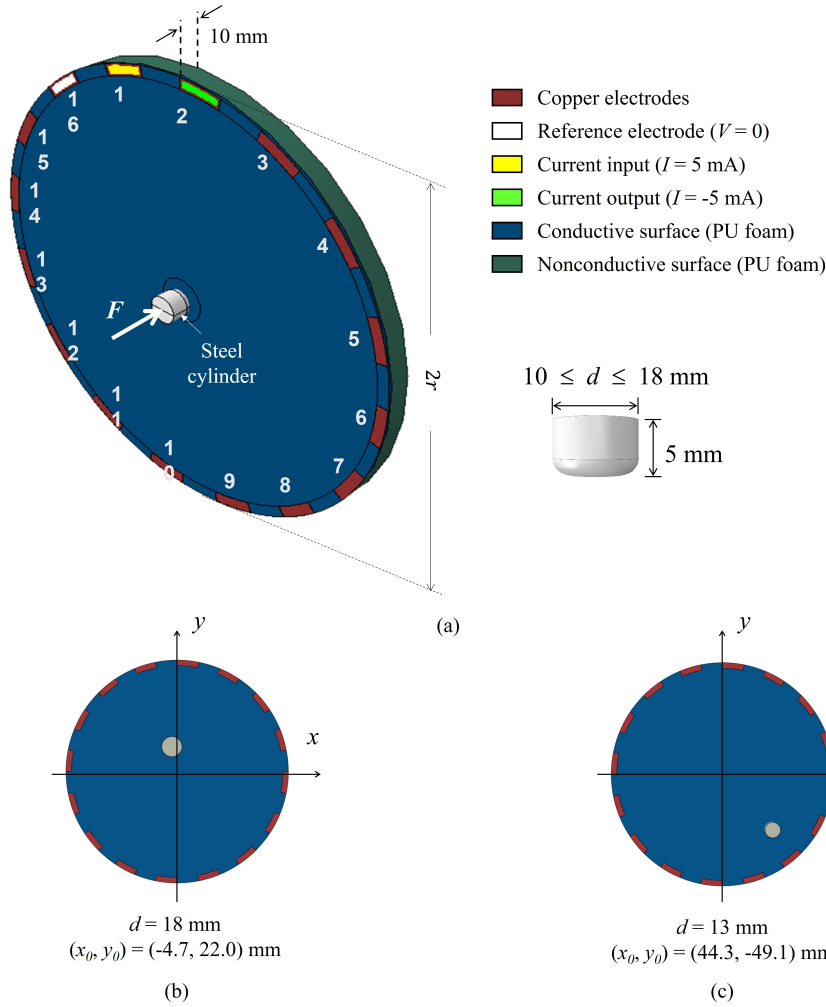


Fig. 7: (a) The FEA model of the EIT sensor domain with the 16 electrodes, (b) and (c) show two cases of random stimulus diameter d and position (x_0, y_0) .

as shown in fig. 6 (b) and (c), and it is subjected to a random compressive force F between 0.1 to 2 N such that it contacts and deforms the EIT sensor. This random assignment and generation of the EIT model shown in fig. 6 is accomplished through a Python script. To model the current injection and ejection patterns, sixteen coupled electric-displacement simulation steps are defined in each run, through the Python script. The script sets an electrode as a current injection electrode with input current $I = 5$ mA and the adjacent one to the right as a current ejection electrode with output current $I =$

-5 mA, e.g. current input and output electrodes in fig. 6 (a). The electrode adjacent to the left of the current input electrode is chosen to have a zero potential boundary condition to act as a reference electrode, e.g. $V = 0$. This assignment of input, output and reference electrodes is repeated in a full cycle around the domain of the EIT sensor such that a total of sixteen patterns are recorded in sixteen different steps for each simulation case with a random value of cylinder diameter d , position (x_0, y_0) and stimulus force F . The bottom surface of the EIT body is prescribed fixed displacement boundary conditions throughout all the steps in each simulation.

A coupled thermal-displacement analysis, using the thermal-electrical analogy, incorporating geometric non-linearity effects, was used to model the behavior of the EIT sensor. The model was fully meshed with hexahedral elements. The EIT sensor's PU foam material was represented by 'C3D8RHT' hourglass-controlled linear displacement-thermal hexahedral elements. The copper electrodes and the cylindrical steel punch were meshed using 'C3D8T' linear hexahedron displacement-thermal elements. Moreover, a mesh convergence study was performed to evaluate the impact of mesh density on the accuracy of the results. The mesh density of the components of the assembly were varied, and the resulting mesh convergence plots for average contact stress and maximum indentation depth for a random loading scenario are shown in Fig. 8. The results indicate that a 63000-element model provided a good balance between accuracy and computation time and was thus selected for subsequent analyses.

To investigate the viscoelastic effect on the model, a viscosity step is introduced, and the model is allowed to relax for different time intervals (2, 5, 60, 120, and 180 seconds) while the current injection patterns are applied across the domain for each time interval. Fig. 9 displays the impact of relaxation on the average contact stress (σ_c^{ave}) and the potential reading for an arbitrary electrode and pattern of choice. A drop of 10 % in average contact pressure is noticeable in the initial time period of relaxation, particularly for touch duration less than 2 seconds, after which an insignificant change in σ_c^{ave} and in potential values are recorded. As a result of these observations and the considerable increase in computational time when accounting for relaxation, the foam's viscoelastic effect was disregarded in the model.

4.5. Finite Element Results

After solving the EIT forward problem simulation for given arbitrary inputs shown in fig. 10, potential readings for each current injection pattern

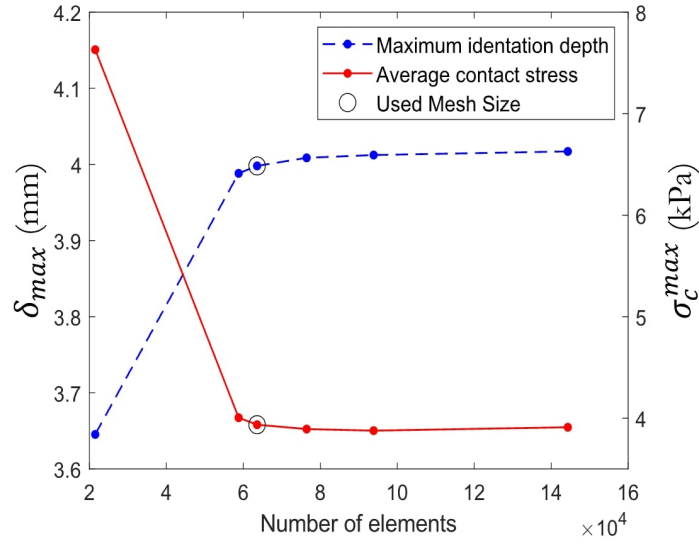


Fig. 8: Mesh convergence study of average contact stress and maximum indentation depth with respect to number of elements used in the EIT model.

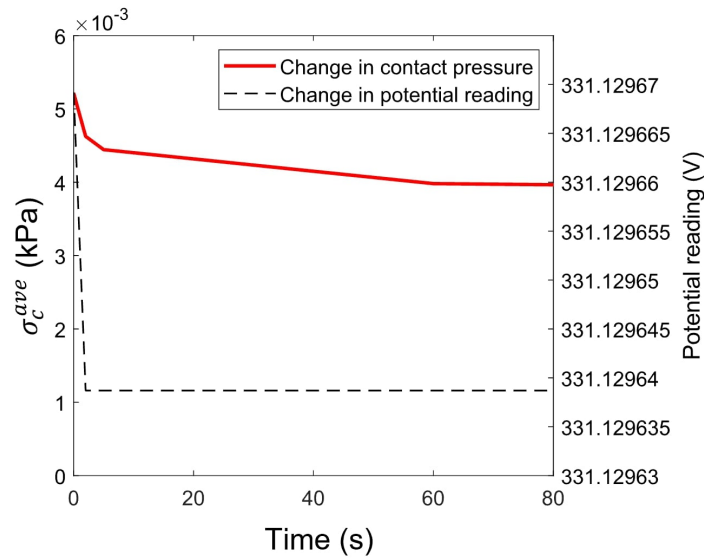


Fig. 9: Effect of relaxation on contact pressure and potential readings.

were obtained for a full cycle around the domain. Furthermore, the voltage readings for each electrode in the full cycle around the domain were extracted,

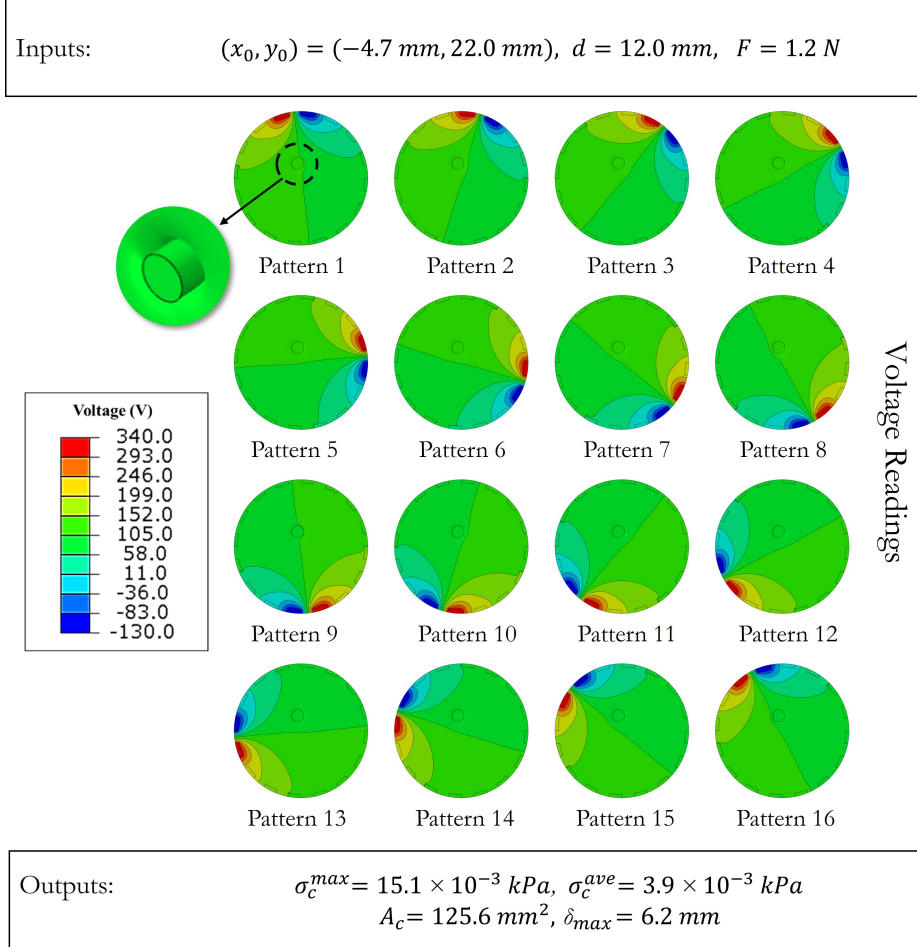


Fig. 10: Potential readings obtained for the 16 current injection patterns of the domain after a touch by a cylindrical steel punch at an arbitrary location.

in a post-process step, by computing the arithmetic average of the voltage for each electrode nodes across all current injection patterns. The extracted voltage readings included 13 voltage values for each injection pattern, excluding the injection and reference electrodes. Thus, a total of 208 voltage readings were obtained for the 16 injection patterns used in this model.

The simulated system produces four mechanical behavior outputs, which are maximum contact stress (σ_c^{max}), average contact stress (σ_c^{ave}), contact area (A_c), and maximum indentation depth (δ_{max}). σ_c^{max} is the highest stress experienced at any point of contact between the punch and the EIT sensor,

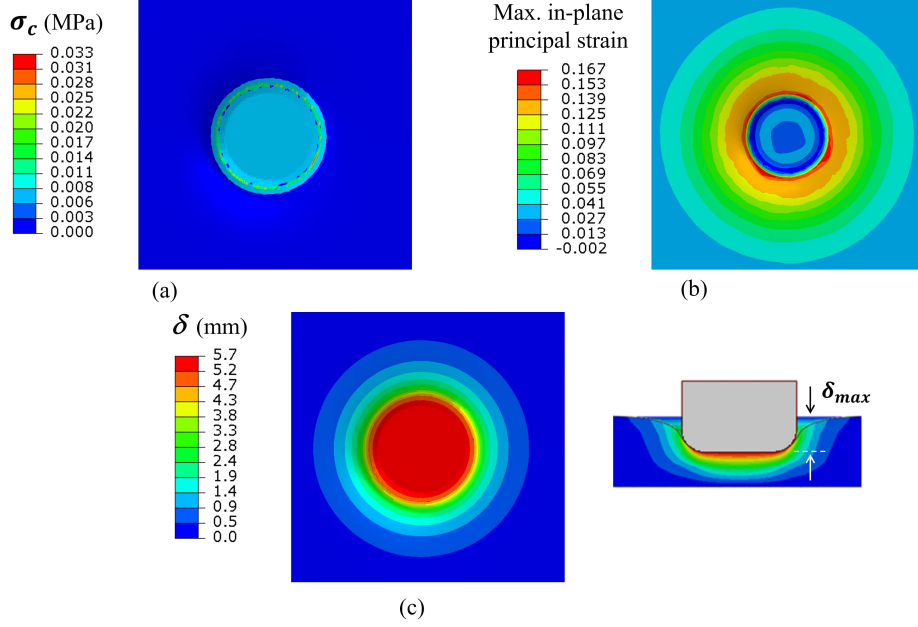


Fig. 11: Tactile response to arbitrary inputs, including (a) contact pressure (σ_c) distribution, (b) maximum in-plane principal strain map, and (c) displacement (δ) map.

while σ_c^{ave} is the average of all stresses at all points of contact. A_c is obtained by summing the surface areas where contact forces exist, and δ_{max} is the highest vertical displacement found in the sensor's body. In fig. 10, the outputs of the mechanical behavior simulations corresponding to the given arbitrary inputs are listed.

Moreover, fig. 11 illustrates the domain's maximum in-plane principal strain contour, the displacement contour (δ), and the contact pressure (σ_c) resulting from the arbitrary inputs, mentioned in fig. 10. It shows that the outer boundaries of the touching punch have the largest strain at the region of contact, while the punch's center has the highest displacement. Furthermore, the contact pressure was found to be the highest where the strain is greatest. The conventional approach to solving the forward EIT problem is to determine the potential distribution in a conductive region. However, these results suggest that the finite element model developed in this study not only solves the forward EIT problem but also provides a comprehensive mechanical response of the system, including contact pressure, contact area, indentation depth, and location of stimulus.

5. Data-Driven Evaluation

5.1. Methodology

In traditional EIT analyses, the primary goal is to map the conductivity distribution from boundary voltage-current data. However, this study shifts focus towards extracting mechanical responses from EIT. A machine learning approach was used to determine the spatial location of contacts and predict the corresponding mechanical response of the sensor. To facilitate this, the developed EIT forward problem model was employed to generate a large dataset. This dataset is then used to train an individual ANNs for each desired output.

The ANNs were structured with an input layer, a hidden layer, and an output layer. The input layer is fed with the voltage readings after being normalized using min-max normalization, which involves scaling the values between 0 and 1 based on the minimum and maximum values in the dataset following Eq. 7,

$$\hat{x} = \frac{(x - x_{min})}{(x_{max} - x_{min})} \quad (7)$$

where \hat{x} is the data point after normalization, x is the desired point to be normalized, x_{min} is the minimum value possible for the data point, and x_{max} is the maximum value possible for the data point. Next, the normalized voltage readings are flattened into a 1×208 vector and the ANN is trained using Bayesian Regularization back-propagation to handle the noisy dataset inherent in EIT systems. The trained ANNs is then tested to predict the mechanical response of the system.

A total of 4000 scenarios were executed using the developed EIT forward problem model with randomized input values of (x_0, y_0) , d , and F . The data extracted from the simulations, to be used for the training of the ANNs, include 208 voltage readings, contact position (x_0, y_0) , punch diameter d , stimulus force F , maximum contact pressure σ_c^{max} , average contact pressure σ_c^{ave} , contact area A_c , and maximum indentation depth δ_{max} . Using voltage data as inputs, eight neural networks predicted the rest of the data as outputs. Fig. 12 illustrates the underlying structure of the machine learning system, which utilizes the proposed finite element model for the forward problem. The study utilized 70 % of the 4000 scenarios as training datasets, 15 % as validation datasets to prevent overfitting, and the remaining 15 %, which were not used in training, were used as testing datasets. During the training and construction of the ANN, the position (x_0, y_0) was normalized

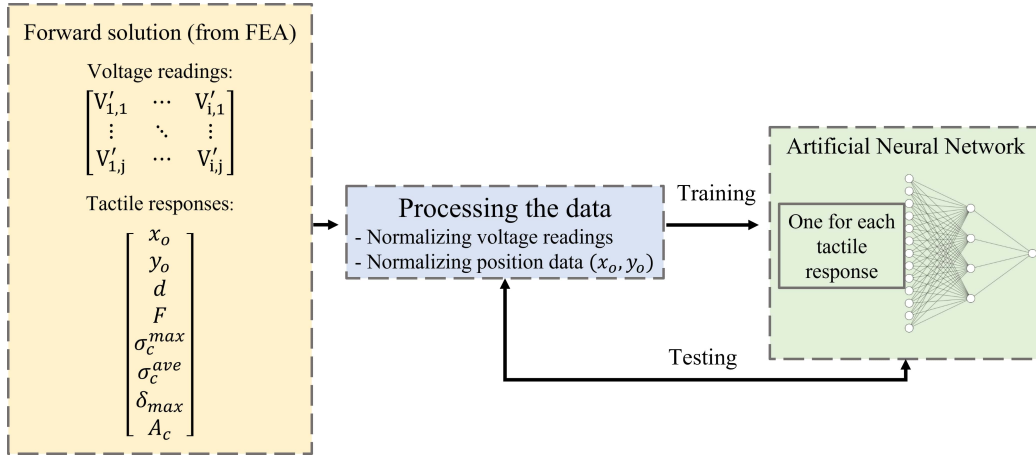


Fig. 12: The structure of the artificial neural network (ANN) used.

with radius of the sensor $r = 100$ mm (see fig. 7(a)) utilizing min-max normalization.

5.2. Results & Discussion

Back-propagation based ANNs are capable of giving accurate results due to their ability of learning from large amounts of data through an iterative process. Through this iterative process, the neural network learns to recognize patterns in the input data and to make accurate predictions based on those patterns. As the network is trained on additional data, it becomes increasingly accurate in its predictions. In this study, two metrics were employed to evaluate the performance of the developed machine learning system. These metrics are the mean squared error (MSE) and the coefficient of determination (R^2) values. MSE measures the average squared difference between the predicted and actual values, with lower values indicating better performance, while R^2 value indicates the proportion of the variance in the target variable, with values closer to 1 indicating a better fit. By employing these metrics, the study provides a comprehensive evaluation of the performance of the developed ANNs, enabling the identification of any areas that require improvement. Figs. 13-19, show the performance of the ANN systems for both the training and testing results, exhibit minimal error represented in both MSE and R^2 values. Overall the R^2 value for all ANNs is larger than 0.9, which is considered an accurate value and demonstrates the ability of the ANNs accurate and precise predictions. Moreover, the MSE

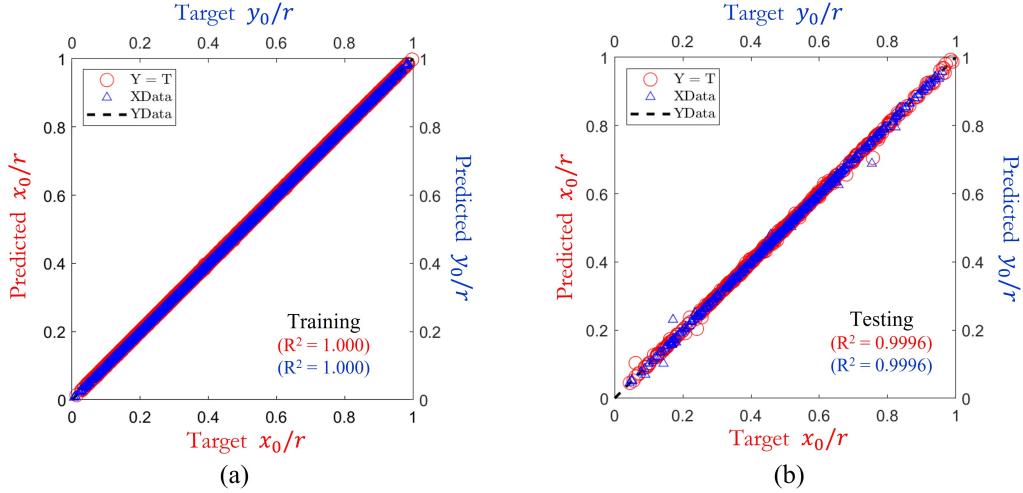


Fig. 13: Normalized coordinates $(x_0/r, y_0/r)$ performance evaluation, e.g. predicted vs. target values: (a) training (MSE = 7.98×10^{-7} mm/mm for x_0 and 5.04×10^{-7} mm/mm for y_0) and (b) testing (MSE = 3.35×10^{-5} mm/mm for x_0 and 3.05×10^{-5} mm/mm for y_0) data.

values for all ANNs are consistent across both the training and validation sets, which suggests that it is not overfitting to the training data and the ANNs are capable of generalizing well to new data. It is interesting to note in Fig. 13(a) that ANN training dataset has a perfect match, e.g. $R^2 = 1.0$, between target and predicted location of the punch, and near to perfect match in the testing dataset Fig. 13(b). The trained ANNs used in the study faces several complexities, including the inherently ill-posed nature of the EIT problem, the effect of geometric non-linearities in the finite element model and the highly non-linear constitutive hyperfoam material model used. Despite those complexities, the touch position (x_0, y_0) predictions in Fig. 13 demonstrated exceptional performance with a very small margin of error. Moreover, the networks responsible for predicting other mechanical behavior outputs exhibit a noteworthy performance.

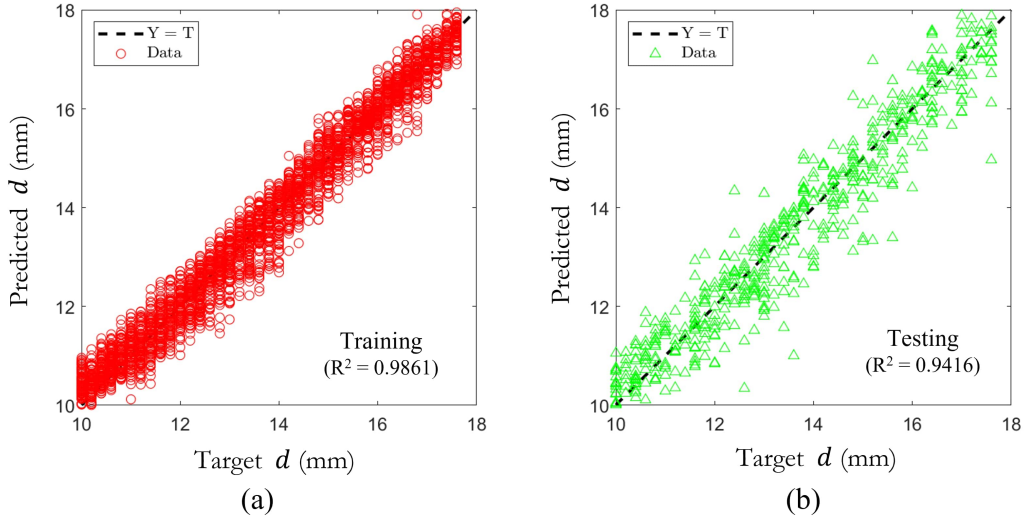


Fig. 14: Punch diameter d performance evaluation, e.g. predicted vs. target values: (a) training (MSE = 0.14 mm) and (b) testing (MSE = 0.56 mm) data.

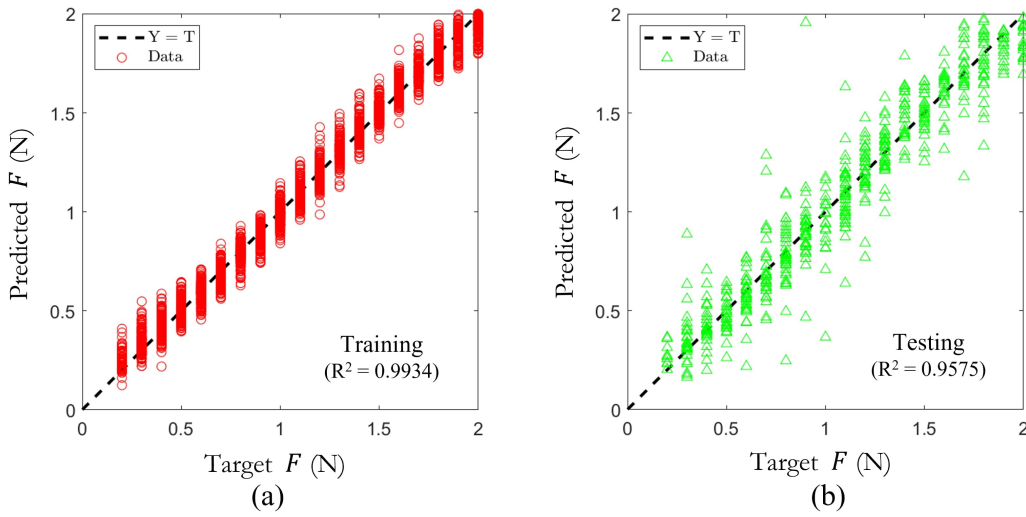


Fig. 15: Stimulus force F performance evaluation, e.g. predicted vs. target values: (a) training (MSE = 3.60×10^{-3} N) and (b) testing (MSE = 2.3×10^{-2} N) data.

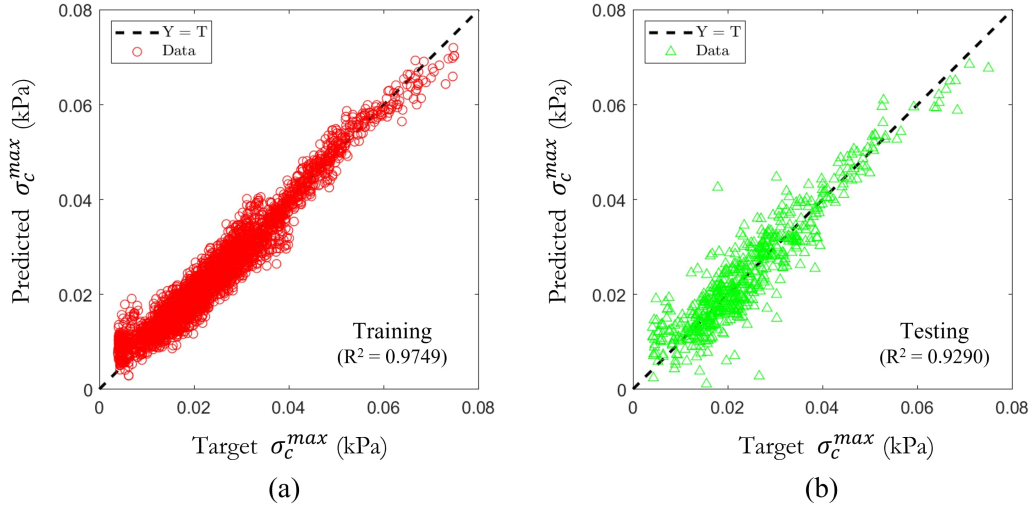


Fig. 16: Maximum contact stress σ_c^{max} performance evaluation, e.g. predicted vs. target values: (a) training (MSE = 8.11×10^{-6} kPa) and (b) testing (MSE = 2.12×10^{-5} kPa) data.

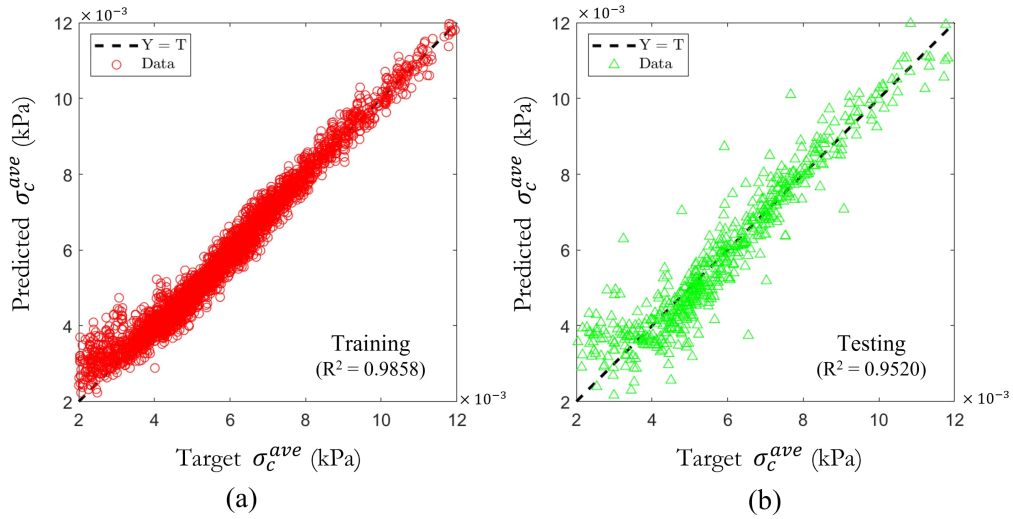


Fig. 17: Average contact stress σ_c^{ave} performance evaluation, e.g. predicted vs. target values: (a) training (MSE = 1.20×10^{-7} kPa) and (b) testing (MSE = 4.27×10^{-7} kPa) data.

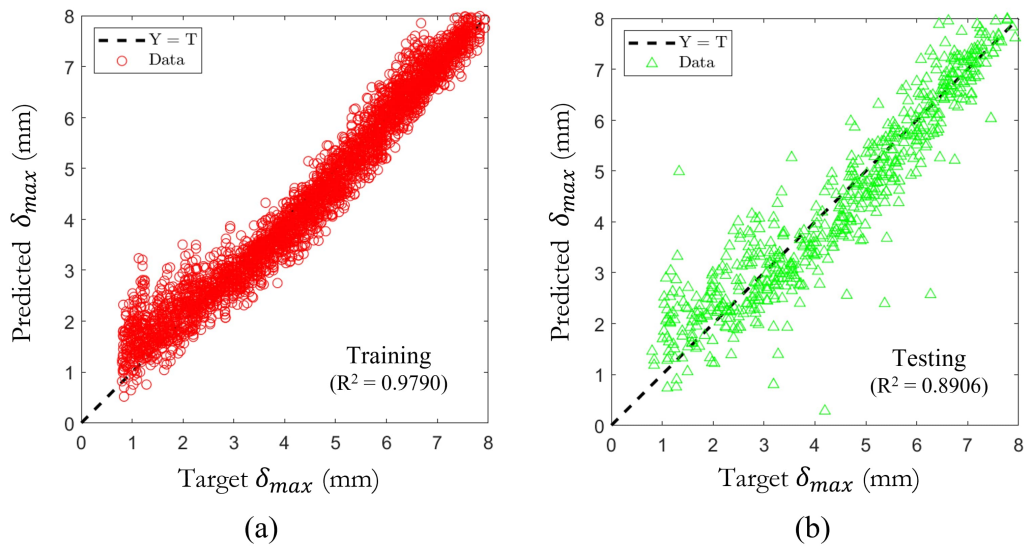


Fig. 18: Maximum indentation depth δ_{max} performance evaluation, e.g. predicted vs. target values: (a) training (MSE = 0.16 mm) and (b) testing (MSE = 0.83 mm) data.

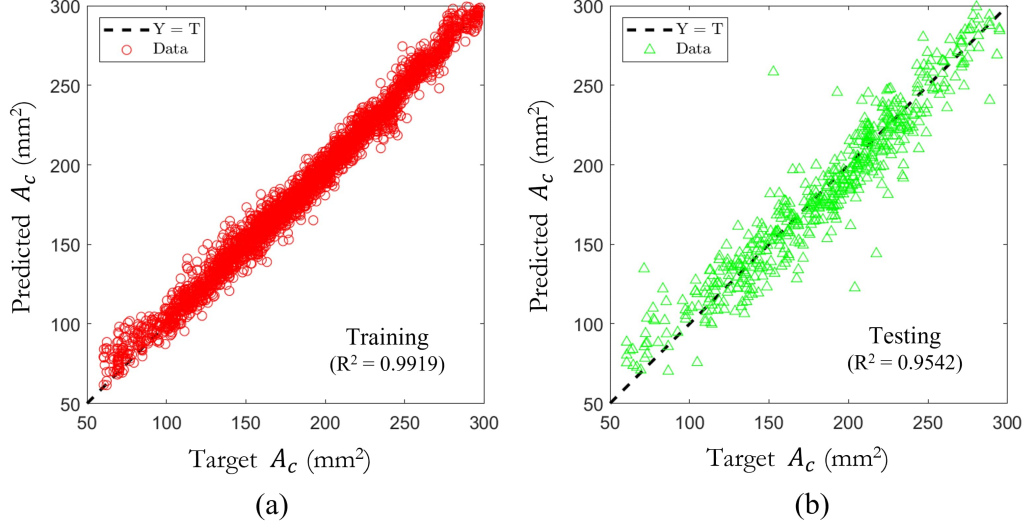


Fig. 19: Contact area A_c performance evaluation, e.g. predicted vs. target values: (a) training (MSE = 49.06 mm²) and (b) testing (MSE = 65.90 mm²) data.

The ANNs responsible for predicting touch intensity (e.g. σ_c^{max} , σ_c^{ave} , and δ_{max}), were found to slightly overestimate these values at their lower range. This could be attributed to the complexity in the highly non-linear hyperfoam constitutive material model used in this study. As an indicator, the ANNs used for predicting touch position (x_0, y_0) show very accurate predictions regardless of touch intensity. This suggests that the overestimation in σ_c^{max} , σ_c^{ave} , and δ_{max} is likely related to the constitutive behavior of the material, rather than any limitations in the ANNs themselves. Moreover, the employed combined hyperfoam model deviates slightly from the actual material behavior at lower stress levels, as illustrated in Figs. 3 (b) and 4 (b). In particular, experimental results indicate that the material is stiffer at lower stress levels compared to the hyperfoam constitutive material model. Thus, for a given strain level the stress values should essentially be slightly higher, which the ANNs typically predict as shown in Figs. 16 and 17 for lower values.

A key strength of the developed framework is its ability to generate training data for the ANNs by solving randomized coupled EIT forward problems through a sophisticated FEA model. This approach not only ensures that the training data covers a wide range of scenarios and conditions but also sig-

nificantly simplifies the process of acquiring training data. Instead of having to gather experimental data manually, which can be both time-consuming and resource-intensive, the framework generates synthetic data efficiently and consistently. This streamlined process not only accelerates the development of the ANNs but also reduces the likelihood of errors or biases introduced by manual data collection. By using this comprehensive and diverse dataset, the ANNs are better equipped to recognize patterns and make accurate predictions even in the presence of noise or previously unseen conditions. The performance of the ANNs, as evidenced by the R^2 values and MSE, demonstrates their ability to make accurate predictions despite these complexities. The successful implementation of Bayesian Regularization back-propagation for handling noisy datasets and the generalizability of the ANNs to new data further underscores the strength of this framework. Moreover, the versatility of the developed methodology allows it to be adapted and applied to other EIT-based sensor systems, making it a valuable contribution to the field. The framework also exhibits potential for refinement and optimization, paving the way for future research to explore alternative machine learning techniques or more advanced ANN architectures to enhance its performance.

The implications of this research are significant, as the developed EIT-based sensor framework has the potential to advance various industries and fields where non-invasive, real-time monitoring of material properties or structural integrity is essential. For example, in the biomedical field, EIT-based sensors could be employed for monitoring blood flow or detecting tumors, while in civil engineering, they could be used to assess the health of infrastructure such as bridges or buildings. Additionally, the framework can be utilized in the field of robotics for tactile sensing, enabling robots to interact more effectively with their environment and improve object manipulation. Instead of traditionally mapping conductivity distribution, the approach presented here utilizes EIT data to extract crucial mechanical properties of the system. By establishing a data-driven approach to EIT analysis and demonstrating its efficacy, this study paves the way for further innovation and application of EIT-based sensors in multiple domains. The potential impact of this technology on improving safety, efficiency, and cost-effectiveness across various sectors highlights the importance of this research and its potential to drive advancements in the years to come.

Though the present study illustrates the potential of the proposed framework, practical validation and application remain areas for future exploration. The work of Zhang et al. [59] and Ross et al. [18] provides promising

initial evidence of the applicability of similar EIT-based sensor systems in real-world scenarios. Additionally, the research conducted by Chen et al. [21] demonstrates the value of a combined elastic FEA and EIT approach. They used this combination to train a neural network that effectively predicted strain and stress, which was corroborated by experimental validation. Their work serves as a valuable foundation and motivation for further investigation and experimentation, paving the way for more comprehensive validation and implementation of the developed framework in various domains.

6. Conclusions

In this study, a numerical modeling framework for developing tactile sensors has been introduced, extending the established applications of mechanics imaging via EIT, predominantly employed in structural health monitoring, into the domain of robotic sensing. This framework utilizes data-driven methods to predict essential mechanical responses, thus expanding our understanding of system behaviour beyond conventional EIT analyses. The mechanical behaviour of polyurethane foam and the effect of strain on conductivity were investigated and modelled using a piezoresistive continuum approach. A coupled electro-mechanical finite element model facilitated the resolution of the EIT forward problem, offering detailed mechanical responses. The forward problem FEA model was then used to generate a large number of random touching scenarios, as a dataset, to feed into different ANNs, resulting in the prediction of touch location and the sensor’s mechanical response with rather high precision. However, the sensor demonstrated certain limitations. Notably, the generation of FEA-based training data necessitated prior knowledge of the sensor’s working conditions. In addition, this study has simplified the EIT analysis by focusing on single point mechanics rather than the conventional full-field solution. Future research could consider wider scenarios, such as multiple stimuli of varying shapes and materials. It is also valuable to explore and compare different data-driven techniques and consider full image reconstruction. Evaluating the performance of the trained ANNs within actual experimental setups under diverse conditions would provide insights into the practical applicability of the developed framework.

CRediT authorship contribution statement

Mohamed Elkhodbia: Conceptualization, Methodology, Formal analysis, Investigation, Writing – original draft/ Review & Editing. Imad Barsoum:

Conceptualization, Resources, Methodology, Writing – review & editing, Supervision, Project administration, Funding acquisition. Feras Korkees: Methodology, Writing – review & editing.

Declaration of competing interest

The authors declare that they have no known competing financial interests or personal relationships that could have appeared to influence the work reported in this paper.

Acknowledgment

The authors acknowledge the financial support provided by Khalifa University.

References

- [1] D. Silvera-Tawil, D. Rye, M. Soleimani, M. Velonaki, Electrical impedance tomography for artificial sensitive robotic skin: A review, *IEEE Sensors Journal* 15 (4) (2014) 2001–2016.
- [2] H. Hassan, T. N. Tallman, Failure prediction in self-sensing nanocomposites via genetic algorithm-enabled piezoresistive inversion, *Structural Health Monitoring* 19 (3) (2020) 765–780.
- [3] H. Dai, G. J. Gallo, T. Schumacher, E. T. Thostenson, A novel methodology for spatial damage detection and imaging using a distributed carbon nanotube-based composite sensor combined with electrical impedance tomography, *Journal of Nondestructive Evaluation* 35 (2016) 1–15.
- [4] A. Fouchard, S. Bonnet, L. Hervé, O. David, Flexible numerical platform for electrical impedance tomography, in: *COMSOL conference*, Grenoble, 2015.
- [5] W. Zhang, D. Li, An instrumental electrode model for solving eit forward problems, *Physiological Measurement* 35 (10) (2014) 2001.
- [6] A. Elsanadedy, Application of electrical impedance tomography to robotic tactile sensing, Carleton University, 2012.
- [7] E. J. Woo, P. Hua, J. G. Webster, W. J. Tompkins, A robust image reconstruction algorithm and its parallel implementation in electrical impedance tomography, *IEEE Transactions on Medical Imaging* 12 (2) (1993) 137–146.

- [8] A. Adler, R. Guardo, Electrical impedance tomography: regularized imaging and contrast detection, *IEEE transactions on medical imaging* 15 (2) (1996) 170–179.
- [9] T. Tallman, K. Wang, An inverse methodology for calculating strains from conductivity changes in piezoresistive nanocomposites, *Smart Materials and Structures* 25 (11) (2016) 115046.
- [10] T. Tallman, S. Gungor, G. Koo, C. Bakis, On the inverse determination of displacements, strains, and stresses in a carbon nanofiber/polyurethane nanocomposite from conductivity data obtained via electrical impedance tomography, *Journal of Intelligent Material Systems and Structures* 28 (18) (2017) 2617–2629.
- [11] D. Smyl, M. Hallaji, A. Seppänen, M. Pour-Ghaz, Three-dimensional electrical impedance tomography to monitor unsaturated moisture ingress in cement-based materials, *Transport in Porous Media* 115 (2016) 101–124.
- [12] M. Hallaji, A. Seppänen, M. Pour-Ghaz, Electrical impedance tomography-based sensing skin for quantitative imaging of damage in concrete, *Smart Materials and Structures* 23 (8) (2014) 085001.
- [13] H. Hassan, T. N. Tallman, A comparison of metaheuristic algorithms for solving the piezoresistive inverse problem in self-sensing materials, *IEEE Sensors Journal* 21 (1) (2020) 659–666.
- [14] L. Chen, A. Gallet, S.-S. Huang, D. Liu, D. Smyl, Probabilistic cracking prediction via deep learned electrical tomography, *Structural Health Monitoring* 21 (4) (2022) 1574–1589.
- [15] X. Duan, S. Taurand, M. Soleimani, Artificial skin through super-sensing method and electrical impedance data from conductive fabric with aid of deep learning, *Scientific reports* 9 (1) (2019) 1–11.
- [16] J. K. Seo, K. C. Kim, A. Jargal, K. Lee, B. Harrach, A learning-based method for solving ill-posed nonlinear inverse problems: a simulation study of lung eit, *SIAM journal on Imaging Sciences* 12 (3) (2019) 1275–1295.
- [17] D. Smyl, D. Liu, Optimizing electrode positions in 2-d electrical impedance tomography using deep learning, *IEEE Transactions on Instrumentation and Measurement* 69 (9) (2020) 6030–6044.
- [18] R. Ross, Y. Hinton, Damage diagnosis in semiconductive materials using electrical impedance measurements, in: 49th AIAA/ASME/ASCE/AHS/ASC Structures, Structural Dynamics, and Materials Conference, 16th AIAA/ASME/AHS Adaptive Structures

- Conference, 10th AIAA Non-Deterministic Approaches Conference, 9th AIAA Gossamer Spacecraft Forum, 4th AIAA Multidisciplinary Design Optimization Specialists Conference, 2008, p. 1936.
- [19] S. J. Hamilton, A. Hauptmann, Deep d-bar: Real-time electrical impedance tomography imaging with deep neural networks, *IEEE transactions on medical imaging* 37 (10) (2018) 2367–2377.
 - [20] Z. Wei, D. Liu, X. Chen, Dominant-current deep learning scheme for electrical impedance tomography, *IEEE Transactions on Biomedical Engineering* 66 (9) (2019) 2546–2555.
 - [21] L. Chen, H. Hassan, T. N. Tallman, S.-S. Huang, D. Smyl, Predicting strain and stress fields in self-sensing nanocomposites using deep learned electrical tomography, *Smart Materials and Structures* 31 (4) (2022) 045024.
 - [22] T. Tallman, S. Gungor, K. Wang, C. E. Bakis, Damage detection and conductivity evolution in carbon nanofiber epoxy via electrical impedance tomography, *Smart Materials and Structures* 23 (4) (2014) 045034.
 - [23] W. Lestari, B. Pinto, V. La Saponara, J. Yasui, K. J. Loh, Sensing uniaxial tensile damage in fiber-reinforced polymer composites using electrical resistance tomography, *Smart Materials and Structures* 25 (8) (2016) 085016.
 - [24] A. Seppänen, M. Hallaji, M. Pour-Ghaz, A functionally layered sensing skin for the detection of corrosive elements and cracking, *Structural Health Monitoring* 16 (2) (2017) 215–224.
 - [25] M. Hallaji, M. Pour-Ghaz, A new sensing skin for qualitative damage detection in concrete elements: Rapid difference imaging with electrical resistance tomography, *NDT & E International* 68 (2014) 13–21.
 - [26] B. R. Loyola, V. La Saponara, K. J. Loh, T. M. Briggs, G. O’Byrne, J. L. Skinner, Spatial sensing using electrical impedance tomography, *IEEE Sensors Journal* 13 (6) (2013) 2357–2367.
 - [27] S. Yan, D. Jia, Y. Yu, L. Wang, Y. Qiu, Q. Wan, Novel strategies for parameter fitting procedure of the ogden hyperfoam model under shear condition, *European Journal of Mechanics-A/Solids* 86 (2021) 104154.
 - [28] S. Shang, W. Zeng, X.-m. Tao, High stretchable mwnts/polyurethane conductive nanocomposites, *Journal of Materials Chemistry* 21 (20) (2011) 7274–7280.
 - [29] A. Nagakubo, H. Alirezaei, Y. Kuniyoshi, A deformable and deformation sensitive tactile distribution sensor, in: 2007 IEEE International

- Conference on Robotics and Biomimetics (ROBIO), IEEE, 2007, pp. 1301–1308.
- [30] S. Merilampi, T. Björninen, V. Haukka, P. Ruuskanen, L. Ukkonen, L. Sydänheimo, Analysis of electrically conductive silver ink on stretchable substrates under tensile load, *Microelectronics Reliability* 50 (12) (2010) 2001–2011.
 - [31] S. Merilampi, T. Laine-Ma, P. Ruuskanen, The characterization of electrically conductive silver ink patterns on flexible substrates, *Microelectronics reliability* 49 (7) (2009) 782–790.
 - [32] B. M. Lee, K. J. Loh, A 2d percolation-based model for characterizing the piezoresistivity of carbon nanotube-based films, *Journal of materials science* 50 (2015) 2973–2983.
 - [33] M. Taya, W. Kim, K. Ono, Piezoresistivity of a short fiber/elastomer matrix composite, *Mechanics of materials* 28 (1-4) (1998) 53–59.
 - [34] A. K. Chaurasia, G. D. Seidel, Computational micromechanics analysis of electron-hopping-induced conductive paths and associated macroscale piezoresistive response in carbon nanotube–polymer nanocomposites, *Journal of Intelligent Material Systems and Structures* 25 (17) (2014) 2141–2164.
 - [35] X. Ren, A. K. Chaurasia, A. I. Oliva-Avilés, J. J. Ku-Herrera, G. D. Seidel, F. Avilés, Modeling of mesoscale dispersion effect on the piezoresistivity of carbon nanotube-polymer nanocomposites via 3d computational multiscale micromechanics methods, *Smart Materials and Structures* 24 (6) (2015) 065031.
 - [36] T. Tallman, K. Wang, An arbitrary strains carbon nanotube composite piezoresistivity model for finite element integration, *Applied Physics Letters* 102 (1) (2013) 011909.
 - [37] C. Cattin, P. Hubert, Piezoresistance in polymer nanocomposites with high aspect ratio particles, *ACS applied materials & interfaces* 6 (3) (2014) 1804–1811.
 - [38] Y. Wang, A. X. Wang, Y. Wang, M. K. Chyu, Q.-M. Wang, Fabrication and characterization of carbon nanotube–polyimide composite based high temperature flexible thin film piezoresistive strain sensor, *Sensors and Actuators A: Physical* 199 (2013) 265–271.
 - [39] A. Firouzeh, A. F. Amon-Junior, J. Paik, Soft piezoresistive sensor model and characterization with varying design parameters, *Sensors and Actuators A: Physical* 233 (2015) 158–168.
 - [40] M. Kim, J. Jung, S. Jung, Y. H. Moon, D.-H. Kim, J. H. Kim, Piezore-

- sistive behaviour of additively manufactured multi-walled carbon nanotube/thermoplastic polyurethane nanocomposites, *Materials* 12 (16) (2019) 2613.
- [41] Rubber, vulcanized or thermoplastic — Determination of shear modulus and adhesion to rigid plates — Quadruple-shear methods, Standard, International Organization for Standardization, Geneva, CH (Aug. 2016).
- [42] Rubber, vulcanized or thermoplastic — Determination of stress relaxation in compression — Part 1: Testing at constant temperature, Standard, International Organization for Standardization, Geneva, CH (Aug. 2019).
- [43] Polymeric materials, cellular flexible - Determination of stress-strain characteristic in compression - Part 1 : Low-density materials, Standard, International Organization for Standardization, Geneva, CH (Aug. 1986).
- [44] C. Briody, B. Duignan, S. Jerrams, J. Tiernan, The implementation of a visco-hyperelastic numerical material model for simulating the behaviour of polymer foam materials, *Computational Materials Science* 64 (2012) 47–51.
- [45] M. Ju, H. Jmal, R. Dupuis, E. Aubry, Visco-hyperelastic constitutive model for modeling the quasi-static behavior of polyurethane foam in large deformation, *Polymer Engineering & Science* 55 (8) (2015) 1795–1804.
- [46] S. Kim, H. Shin, S. Rhim, K. Y. Rhee, Calibration of hyperelastic and hyperfoam constitutive models for an indentation event of rigid polyurethane foam, *Composites Part B: Engineering* 163 (2019) 297–302.
- [47] J. Kost, M. Narkis, A. Foux, Effects of axial stretching on the resistivity of carbon black filled silicone rubber, *Polymer Engineering & Science* 23 (10) (1983) 567–571.
- [48] J. Kost, M. Narkis, A. Foux, Resistivity behavior of carbon-black-filled silicone rubber in cyclic loading experiments, *Journal of applied polymer science* 29 (12) (1984) 3937–3946.
- [49] J. Kost, A. Foux, M. Narkis, Quantitative model relating electrical resistance, strain, and time for carbon black loaded silicone rubber, *Polymer engineering & science* 34 (21) (1994) 1628–1634.
- [50] E. Sevkat, J. Li, B. Liaw, F. Delale, A statistical model of electrical resistance of carbon fiber reinforced composites under tensile loading, *Composites Science and Technology* 68 (10-11) (2008) 2214–2219.

- [51] A. Adler, W. Lionheart, N. Polydorides, Eidors: electrical impedance tomography and diffuse optical tomography reconstruction software.
- [52] S. Nonn, M. Schagerl, Y. Zhao, S. Gschossmann, C. Kralovec, Application of electrical impedance tomography to an anisotropic carbon fiber-reinforced polymer composite laminate for damage localization, *Composites Science and Technology* 160 (2018) 231–236.
- [53] D. Systèmes, Abaqus analysis user’s guide (6.14) dassault systèmes, Vélizy-Villacoublay, France (2014).
- [54] J. S. Bergstrom, *Mechanics of solid polymers: theory and computational modeling*, William Andrew, 2015.
- [55] R. W. Ogden, Large deformation isotropic elasticity—on the correlation of theory and experiment for incompressible rubberlike solids, *Proceedings of the Royal Society of London. A. Mathematical and Physical Sciences* 326 (1567) (1972) 565–584.
- [56] C. Renaud, J.-M. Cros, Z.-Q. Feng, B. Yang, The yeoh model applied to the modeling of large deformation contact/impact problems, *International Journal of Impact Engineering* 36 (5) (2009) 659–666.
- [57] G. A. Holzapfel, *Nonlinear solid mechanics: a continuum approach for engineering science* (2002).
- [58] J. Soussou, F. Moavenzadeh, M. Gradowczyk, Application of prony series to linear viscoelasticity, *Transactions of the Society of Rheology* 14 (4) (1970) 573–584.
- [59] Y. Zhang, G. Laput, C. Harrison, Electrick: Low-cost touch sensing using electric field tomography, in: *Proceedings of the 2017 CHI Conference on Human Factors in Computing Systems*, 2017, pp. 1–14.